Published in final edited form as:
Ultrason Imaging. 2009 July ; 31(3): 201–213.

In Vivo Cardiac, Acoustic-Radiation-Force-Driven, Shear Wave Velocimetry

Richard R. Bouchard, **Stephen J. Hsu**, **Patrick D. Wolf**, and **Gregg E. Trahey**
Department of Biomedical Engineering, Duke University, Durham, NC

Richard R. Bouchard: rrb@duke.edu; Stephen J. Hsu: ; Patrick D. Wolf: ; Gregg E. Trahey:

Abstract

Shear wave elasticity imaging (SWEI) was employed to track acoustic radiation force impulse (ARFI) -induced shear waves in the mid-myocardium of the left ventricular free wall (LVFW) of a beating canine heart. Shear waves were generated and tracked with a linear ultrasound transducer that was placed directly on the exposed epicardium. Acquinsition was ECG-gated arid coincided with the mid-diastolic portion of the cardiac cycle. Axial displacement profiles consistent with shear wave propagation were clearly evident in all SWEI acquisitions (i.e., those including an ARFI excitation); displacement data from control cases (i.e., sequences lacking an ARFI excitation) offered no evidence of shear wave propagation and yielded a peak absolute mean displacement below 0.31 μm after motion filtering. Shear wave velocity estimates ranged from 0.82 to 2.65 m/s and were stable across multiple heartbeats for the same interrogation region, with coefficients of variation less than 19% for all matched acquisitions. Variations in velocity estimates suggest a spatial dependence of shear wave velocity through the mid-myocardium of the LVFW, with velocity estimates changing, in limited cases, through depth and lateral position.

Keywords

Acoustic radiation force; cardiac imaging; myocardium; shear wave velocimetry; ultrasound

I. INTRODUCTION

Acoustic-radiation-force-generated shear waves

Acoustic radiation force is applied to absorbing or reflecting targets in the propagation path of an acoustic wave. This phenomenon is caused by a transfer of momentum from the acoustic wave to the propagation medium. The spatial distribution of the radiation force field is determined by both the transmitted acoustic parameters and tissue properties. The contribution due to tissue absorption is in the direction of wave propagation, whereas the contribution due to scattering is dependent upon the angular scattering properties of the target. In the event that the target has an axis of symmetry perpendicular to the direction of wave propagation (e.g., the target is spherical), the radiation force due to scattering is entirely in the direction of wave propagation. In this situation, the radiation force, F, is given by:

$$F = \left(\Pi_a + \Pi_s - \int \gamma \cos\theta r dr d\theta\right) \langle E \rangle \quad (1)$$

Correspondence to: Richard R. Bouchard, rrb@duke.edu.

where Π_a is the total power absorbed by the target, Π_s, is the total power scattered by the target, γ is the magnitude of the scattered intensity, θ is the scattering angle, $rdrd\theta$ is an area element of the projection of the target onto the axial/lateral plane and $\langle E \rangle$ is the temporal-average energy density of the propagating acoustic wave.[1]

For a focused acoustic beam with a center frequency and focus typical of diagnostic imaging, the force is effectively applied from the probe surface to just beyond the focal region of the acoustic beam when propagating through soft tissue. The dynamic response resulting from this induced force can be analyzed for the purpose of tissue elasticity imaging. Such an approach is taken in Acoustic Radiation Force Impulse (ARFI) imaging, which analyzes certain displacement metrics (e.g., peak displacement, the time to this peak) within the excitation beam volume for the purpose of assessing tissue stiffness.[2] Along with localized displacement within the region of ultrasonic beam propagation, an ARFI excitation produces shear waves that propagate in the direction transverse to the direction of longitudinal wave propagation. Sarvazyan et al first envisioned using impulsive radiation force to remotely generate shear waves and to quantify tissue stiffness based upon wave propagation speed in their initial implementation of shear wave elasticity imaging (SWEI).[3] The velocity of generated shear waves has been shown to be reflective of tissue's shear modulus.[4] In a linear, isotropic, elastic medium, the speed of these shear waves (c_T) can be expressed as:

$$c_T = \sqrt{\frac{\mu}{\rho}} = \sqrt{\frac{E}{2(1+\nu)\rho}} \tag{2}$$

where μ is the shear modulus, E is the Young's modulus, ν is the Poisson's ratio, and ρ is the density of the tissue. A typical range for shear wave velocities in soft tissue is 1 to 5 m/s.[5]

Current ARFI-based SWEI research tends to focus on fairly isotropic tissues. Bercoff et al developed a specific implementation of SWEI, known as supersonic shear imaging, which allows for an increased depth of field (DOF) by transmitting consecutive ARFI excitations that are focused at varied depths.[6] Using this imaging technique, Tanter et al were able to assess elements of breast lesion viscoelasticity *in vivo*.[7] Employing a method with a single-focus excitation that utilized the Lateral Time-to-Peak (TTP) algorithm (which was used in this study and is explained in more detail later), Palmeri et al were able to estimate the shear moduli of human livers *in vivo*.[8]

Cardiac elasticity imaging techiniques

There are several ultrasound-based techniques that can noninvasively assess myocardial function and elasticity. Strain and strain-rate imaging allows one to monitor regional deformations in myocardium with diagnostic ultrasound methods; this deformation information can then be used to assess particular elements of myocardial function.[9, 10] Using ARFI imaging (and thus investigating dynamics *within* the excitation volume), Hsu et al were able to assess the myocardial function of an *in vivo* canine heart.[11] Using these same techniques, they also predicted a cyclic stiffness variation throughout the mid-myocardium that was correlated to the animal's ECG trace, with a state of increased stiffness suggested during systole (when compared to diastole).

Multiple groups have studied low-frequency (< 500 Hz) mechanical wave propagation in the heart for the purpose of investigating elastic properties of myocardium *in vivo*. Researchers have typically focused on naturally-occurring or externally-generated waves while tracking methods have utilized both ultrasound- and MRI-based techniques. Many researchers have also characterized the dispersive (i.e., dependence of wave velocity on excitation frequency)

nature of these waves. Kanai first investigated mechanical waves that were generated by the transient dynamics of aortic valve closure.[12] He measured wave speeds in the intraventricular septum (IVS) of 2.0, 4.0, and 4.5 m/s for 27-, 60-, and 87-Hz components, respectively. Citing a wavelength that was larger than the IVS wall thickness, Kanai used a mechanical model based on Lamb wave (a transverse plate mode) propagation to derive additional viscoelastic metrics (e.g., viscosity). Although a different wave propagation mechanism than that observed in this study, Pernot et al employed ultrasound-based techniques to measure the *electromechanical* wave (resulting from propagation of the depolarization wave) that travels through the IVS.[13] At end-systole, they measured wave speeds of 1.20, 3.02, and 4.21 m/s for 82-, 246-, and 410-Hz components, respectively; at beginning-systole, they measured a wave speed of 0.44 m/s for the 230-Hz component. If a low-frequency (typically < 100 Hz) external harmonic excitation is coupled into the heart, it is possible to implement an MRI-based elasticity imaging technique (known as 'MRE'). Sack et al induced 24-Hz shear waves in the IVS of a human heart with an external rod to measure a shear modulus variation ratio of 6.3±0.9 from systole-to-diastole in human cardiac tissue.[14]

II. METHODS

Experimental set-up and methods

The ARFI-based SWEI sequence implemented in this study requires that an ARFI excitation be transmitted to an ROI within a target tissue. The resulting dynamic response then generates shear waves, which induce axial displacement at lateral beam locations away from the excitation center. Relying on beams offset from the ARFI excitation beam, one is then able to track this shear wave response at multiple, offset beam locations. Through the evaluation of these tracking data, which are averaged through a certain depth (i.e., the height of the kernel), it is possible to estimate the average speed of this generated (shear) wavefront through the full extent of all lateral beam locations used in the tracking analysis (i.e., the width of the kernel). To this end, experiments were implemented on a SONOLINE Antares™ ultrasound system using a VF10-5 linear array (Siemens Healthcare, Ultrasound Business Unit, Mountain View, CA) operating at 5.7 MHz. The array was used to both generate and track shear wave propagation, as previously detailed by Palmeri et al.[8] Given that the system cannot track all of its available lateral beam locations simultaneously, the employed shear wave imaging scheme obtains a complete shear wave response of a given lateral extent (typically 2–3 mm) through superposition of the responses from multiple ARFI excitations, which are tracked at four (the system's current limit) distinct lateral locations simultaneously through parallel-receive beamforming. Parallel-receive beamforming allows for an increased frame rate with a minimal reduction in tracking accuracy.[15, 16] Considering the acquisition time needed for this scheme (~20 ms), its implementation was limited to mid-diastole (shortly before the p-wave), a period of reduced physiologic motion.[17] Matched ECG and SWEI acquisition trigger traces were recorded offline to confirm the aforementioned triggering was achieved. Tracked shear waves were created with a 70-μs ARFI excitation pulse in all experimental trials.[2]

The dynamic response resulting from an ARFI excitation was obtained by transmitting repeated B-mode pulses at a specific lateral beam location and using a correlation-based delay estimator (800-μm kernel length) to estimate the delay between the resulting radiofrequency (rf) traces and a pre-ARFI (or 'reference') rf trace.[18] Only displacement estimates with correlation coefficients greater than 0.85 were utilized for shear wave velocimetry analysis. This process was repeated for multiple tracking kernels throughout the DOF and for each sampled lateral location. These displacement data were then processed with a motion-filtering algorithm, intended to mitigate effects of physiological motion. The motion filter assumes physiological motion is of constant acceleration during the sequence acquisition period and that the tissue

fully recovers from the ARFI excitation after a set time. Specific details regarding the implementation of this motion filter are given by Hsu et al.[19]

To estimate shear wave velocity, our research colleagues developed a time-of-flight method, the Lateral TTP algorithm, that tracks peak shear wave-induced displacement as a function of a tracking beam's lateral distance from the excitation focus.[8] In short, TTP (i.e., the time taken to achieve peak displacement) points of motion-filtered displacement profiles (e.g., blue traces in figure 3) are plotted as a function of the lateral position of their respective tracking beams. A linear regression fit is then performed on the TTP displacement versus lateral position data; the inverse slope of this regression fit yields the estimated shear wave velocity for that spatial kernel (e.g., yellow box in figure 2). The square of a fit's correlation coefficient (i.e., *R*-squared value) is calculated to indicate its degree of linearity, with $R^2 = 1$ indicating perfectly linear data.

Study protocol

An open-chest preparation canine study, approved by the Institutional Animal Care and Use Committee at Duke University and conforming to the Research Animal Use Guidelines of the American Heart Association, was performed. The mongrel dog was approximately 20 kg in mass and had a heart rate of 92 bpm. ECG gating was utilized to ensure that acquisition coincided with the mid-diastolic portion of the cardiac cycle. In an effort to mitigate lateral motion, the ultrasound transducer was attached to a vacuum-driven coupling device (Fig. 1b) with an Aquaflex® ultrasonically-transparent, 10-mm standoff (Parker Laboratories, Fairfield, NJ) placed between the heart and the transducer.[19] Following a left thoracotomy, the pericardium was opened and the transducer and attached vacuum-coupling device were placed directly on the exposed epicardium (Fig. 1); the transducer's long axis was approximately aligned with the long axis of the heart. Shear waves were generated and tracked in the mid-myocardium of the left ventricular free wall (LVFW). The transmit focus was 17.5 mm, which was approximately 7.5 mm beyond the distal border of the standoff.

Figure 2 shows a B-mode image of the sampled regions, which were all located in the mid-myocardium of the LVFW. It is important to note that each sampled region contains 14 lateral tracking beams. In the first experiment ('Same Location' experiment), seven acquisitions were obtained in the same location (region 'e' in figure 2) across seven consecutive heartbeats. This acquisition sequence was then repeated with zero-amplitude (or 'no-push') ARFI excitations as a means to assess the efficacy of the physiological motion filter (Fig. 3). In the second experiment ('Different Locations' experiment), seven acquisitions were obtained at six different lateral regions (regions 'a' through 'f' in figure. 2) across seven consecutive heartbeats. There is a combined 46% overlap between a region and its flanking regions (e.g., a 38% overlap between regions 'd' and 'a' and an 8% overlap between regions 'd' and 'b'). Consequently, only alternating, independent regions (e.g., regions 'a' through 'c' and 'd' through 'f') were directly compared. The first sampled region, 'a', was sampled again at the end of the sequence to assess measurement drift. For each acquisition region, velocimetry estimates were obtained for three nonoverlapping kernels through depth (i.e., depth kernels 1 through 3 in figure 2), yielding a total of eighteen spatial kernels. Experiments were performed within a few minutes of one another.

III. RESULTS

As an initial validation, the shear wave acquisition sequence implemented in the following studies was tested on a calibrated phantom. Shear waves were generated in and tracked through a homogeneous tissue-mimicking phantom (CIRS, Norfolk, VA) with an independently-validated Young's modulus of 4.5 kPa. After processing, the data obtained from these sequences yielded a velocity estimate of 1.30±0.4 m/s. Solving for the Young's modulus using

Eq. (2) (and assuming $\rho = 1$ g/cm^3 and $\nu = 0.5$) yields an estimate of 5.07 kPa, a 12% difference from the expected value. In the phantom study, this estimate showed no depth dependence throughout the analyzed DOF (which was the same depth range as that employed in all experimental trials).

To assess the efficacy of the motion filter, filtered displacement data obtained from sequences with and without (i.e., 'no-push') active ARFI excitations were compared. Figure 3 presents nonmotion-filtered (a) and motion-filtered (b) displacement data obtained from kernel e-2 (i.e., the second depth kernel from region 'e' in figure 2). In the cases with active ARFI excitations (blue traces), the means of the traces suggest shear wave propagation, with displacement peaks occurring later in time and with decreased amplitude for more distal lateral tracking locations. In the 'no-push' case (red traces), the greatest absolute mean displacement and standard deviation through all time for all four traces is 0.31 and 0.73 μm, respectively, for the filtered data (b) and 6.89 and 11.74 μm, respectively, for the nonfiltered data (a).

Figure 4 presents displacement images from region 'e'. ARFI excitations were transmitted at the leftmost portion of each image (−0.3 to 0.2 mm); the induced displacement wave then propagated from left to right. The upper, leftmost image (A) shows induced displacement one millisecond after initiation of the ARFI excitation. Images B through D then show progressively later (5, 13, and 21 ms, respectively) depictions of this dynamic response. If each lateral sampling location (−0.3 to 2.2 mm) is averaged axially through respective depth kernel regions, the peak averages shown in table 1 result.

Shear wave velocity estimates are detailed for the two experiments in tables 2 and 3. Velocity estimates based on linear fits with *R*-squared values below 0.70 were omitted from statistical analysis and replaced with a dash mark. This threshold was established through a qualitative assessment of the linearity of TTP data from physiologic data sets; it was chosen as an approximate point at which jump discontinuities (e.g., suggesting physically unlikely wavefront accelerations) were observed in the data. Table 2 presents velocity estimates from the Same Location experiment. Estimates for a single region ('e') from three depth kernels across seven heartbeats are shown. Velocity estimates range from 0.83 to 2.64 m/s and are based on motion-filtered data. The mean value of velocities for the shallowest depth kernels (1 and 2) are within 1% of each other while the mean velocity for the deepest depth kernel (3) is approximately double either of the other two. The coefficients of variation (i.e., σ/μ) between the estimates at each depth are 5.1, 10.0, and 18.7% for depth kernels 1,2, and 3, respectively. The greatest difference observed between any two consecutive (temporally) kernels at the same depth is 26.2% (depth2, heartbeats 2 and 3); the least difference between consecutive kernels is 0.2% (depth 1, heartbeats 4 and 5); the average absolute difference between all consecutive kernels is 9.5%.

Mean *R*-squared values for the three depth kernels ranges between 0.91 and 0.95, which indicates, on average, a fairly high degree of linearity in the data used in the regression fit; the lowest *R*-squared value among all 20 estimates is 0.71 (denoted with an asterisk). For the sake of comparison, shear wave velocity was estimated for nonmotion-filtered displacement data from the Same Location experiment; these estimates were then compared to those obtained from corresponding motion-filtered data. In the cases when *R*-squared values for the nonfiltered data are greater than 0.70, the mean ($N = 8$) and standard deviation of the absolute differences between the two groups (i.e., filtered vs. nonfiltered) is 4.9 ± 6.7%, with the maximum difference being 20.9%. Estimates based on nonfiltered data tended to be higher than estimates based on filtered data. For the other twelve estimates (i.e., $R^2 \leq 0.70$), the mean absolute difference is 40.4% while estimated velocities range from 0.24 to 14.3 m/s.

Table 3 presents shear wave velocimetry estimates from the Different Locations experiment. Velocity estimates for six locations (regions ‘a’ through ‘e’ from figure 2) are presented for three depth kernels. Bolded and italicized fonts denote sets of nonoverlapping regions; there are 3 mm between centers and 1.1 mm between proximal boundaries of adjacent kernels in each set for a given depth. Shear wave velocity estimates range from 0.82 to 2.65 m/s. The greatest difference (i.e., greatest velocity compared to least velocity) through depth at a single lateral position was observed in region ‘a’, which has a difference of 42.2%; the smallest difference was observed in region ‘b’, with a difference of 14.1%. The greatest difference between adjacent but nonoverlapping kernels at a fixed depth was observed between kernels e-1 and f-1, which yielded a difference of 74.3%; the smallest difference was observed between kernels b-2 and c-2, which have a difference of 27.1%. The differences between velocity estimates from region ‘a’ during the first heartbeat and those during the seventh heartbeat are 12.2, 2.4, and 1.6% for depth kernels 1, 2, and 3, respectively. The lowest *R*-squared value for any estimate presented for this experiment is 0.72 (denoted with an asterisk). All other *R*-squared values were above 0.78, with a mean ($N = 18$) and standard deviation of 0.86 ± 0.06. In comparing estimates from region ‘e’ between the two experiments (mean from Same Location data vs. Different Locations data), differences of 18.8 and 38.1 % were observed for kernels e-1 and e-2, respectively.

IV. DISCUSSION

We have demonstrated in an *in vivo* experiment the ability to generate and track shear waves in myocardium with ultrasound-based methods. Shear wave velocity estimates range from 0.82 to 2.65 m/s, which is similar to wave speed ranges cited for other studies.[12,13] Estimates at a fixed location were quite stable over multiple heartbeats, with coefficients of variation between matched estimates all less than 19%. When the sample location was shifted, however, significant differences in velocity estimates were observed in some cases. In the Same Location (table 2) and Different Locations (table 3) data, a shear wave velocity depth dependence is suggested. The Different Locations data also support a dependence of shear wave velocity on lateral position. Using a linear model to fit the displacement data, for the kernel size cited, appeared appropriate, with *R*-squared values typically greater than 0.9.

Results from the Same Location study demonstrate the stability of the measurement while suggesting a depth dependence of the shear wave velocity. Through a depth of only 1.6 mm (kernel center-to-center distance), a significant increase in velocity was observed from depth 2 to depth 3. Such a dependence could be a result of accompanying changes in myocardial fiber orientation with depth, as discussed in detail below. Results from the Different Locations study also suggest a spatial dependence, with velocity changes observed with lateral and axial kernel shifts. In the most extreme cases, lateral but nonoverlapping kernels yielded velocity estimates with differences of as much as 42.2 and 74.3% for depth and lateral shifts, respectively, of only a few millimeters. Additionally, there appeared to be minimal spatial drift from the first heartbeat to the seventh heartbeat, with differences (comparing velocity estimates from heart beat 1 to heartbeat 7) near the average difference (9.5%) observed with consecutive kernels in the Same Location study.

Comparison of velocity estimates based on nonmotion-filtered versus motion-filtered data (Fig. 3) suggests that motion filtering has little impact on velocity estimation in some cases (8 of 21). In the cases in which it does significantly affect estimation, this generally occurred for one of two reasons, depending on whether the physiological motion is positive (i.e., away from the transducer face) or negative. In the case when it is positive, physiological motion can cause the peak displacement estimate for multiple lateral locations to occur at the conclusion of the sampling period; this introduces artifactual TTP estimates into the linear regression fit. In the case when physiological motion is negative (as is the case presented in figure 3a), the shear

wave-induced peak of a location can be attenuated to the point that it is smaller in magnitude than preceding elements of the displacement trace. An earlier 'peak' is detected instead, which results in a TTP estimate that is lower than expected. Inaccurate TTP values — from the aforementioned sources or estimation jitter — result in reduced *R*-squared values during the linear regression fit portion of the velocity estimation algorithm. Additionally, changes in shear wave velocity within a kernel can also result in reduced *R*-squared values. In the latter case, it is often necessary to reduce the lateral extent of the kernel in order to increase the overall linearity of the data (TTP vs. lateral position).

Previous applications of ARFI-driven shear wave velocimetry have utilized shear wave velocities to estimate a tissue's Young's modulus using the relationship presented in Eq. (2). This relationship, however, is only valid for linear, elastic, isotropic materials. In the case of myocardial tissue, there are many confounding effects that would preclude the implementation of such a straightforward approach. For example, the type of mechanical wave itself could be questioned. Although the observed transverse wave is referred to as a 'shear' wave throughout this text, we are confident only in it being a transverse mechanical wave. The observed phenomenon could be another wave type: a Lamb wave. Kanai employed a Lamb wave model for the purpose of elastic modulus reconstruction through the IVS.[12] In certain cases, when a perturbation (e.g., an ARFI excitation) exists near interfaces of materials with drastically-varying density, it is possible to generate transversely-traveling waves that are not shear waves. Two such wave modes are surface (Rayleigh) and plate (Lamb) waves, which propagate along or between material interfaces, respectively.[20] Although the velocity of these waves is still dependent on material stiffness, other material properties and boundary conditions (e.g., plate thickness) can have a significant influence as well.

Another confounding effect is the inhomogeneity of cardiac tissue, which has a high degree of structural anisotropy. In histological studies, Streeter et al found that the fiber orientation in the LVFW of canine hearts changes across the wall.[21] They also found that the degree of rotation is not constant with depth, noting that the greatest fiber rotation occurred at the epicardial and endocardial tissue surfaces and significantly less rotation occurred in the mid-myocardial portion of the tissue. Anisotropy in the propagation medium is significant as it can have a profound effect on resulting shear wave velocities. Gennisson et al investigated the anisotropy in shear wave propagation parallel and perpendicular to the direction of skeletal muscle fibers.[22] They measured parallel-to-perpendicular shear wave velocity ratios of 2.8 and 4.0 for excised bovine muscle and *in vivo* human bicep muscle, respectively. In regards to the study presented herein, although both data sets suggest depth dependences, the reduced fiber rotation that occurs in the mid-myocardial layer could explain why a more significant depth dependence was not observed (e.g., between depths 2 and 3 in the Same Location experiment). It must be noted, however, that the precise orientation of the velocity estimation kernels (i.e., yellow and cyan boxes in figure 2) relative to the myocardial fiber planes was unknown and could make a direct investigation into this phenomenon difficult.

As mentioned previously, many researchers have studied the dispersive nature of mechanical waves traveling through myocardium. Tanter et al observed substantial dispersion of ARFI-generated shear waves in breast tissue, which is known to be fairly isotropic but viscoelastic.[7] They observed average shear wave phase velocities below 3 m/s for frequencies below 100 Hz while measuring mean velocities in excess of 8 m/s for frequencies above 400 Hz. Additionally, Deffieux et al found that the dispersion of shear wave velocities in skeletal muscle could be highly dependent on fiber orientation.[23] They reported no significant velocity dispersion along (parallel to) muscle fibers but measured strong dispersion, with phase velocities ranging from 0.5 to 2.0 m/s between 75 and 500 Hz, perpendicular to the fiber direction. Thus, a characterization of the ARFI-excitation frequency used in this study and a

subsequent analysis of wave velocities at specific frequencies within this bandwidth could be fruitful in achieving a more complete material characterization of myocardium.

Aside from the aforementioned confounding effects, sources of error in generating and tracking an induced shear wave can also originate from other, perhaps more fundamental, sources. Generation of the shear wave-inducing excitation can be hampered by the substantial reflection and subsequent loss of acoustic energy that occurs at the standoff-epicardial boundary. Also, the ability to track wave peaks at greater depths throughout the DOF also affects shear wave velocity estimate reliability. In the Same Location (table 2) data, the variance of velocities (at a specific depth) increases with depth. As demonstrated in figure 4, ARFI-induced displacement decreased with increased depth, which would indicate a poorer signal-to-noise ratio in the more distal regions. In addition, inadvertent transducer 'tilting' (i.e., pitch and yaw) can result in aberrant (lateral) motion that tends to increase in magnitude with increasing ROI depth. Such motion can lead to signal decorrelation (which affects displacement estimation reliability) and kernel misregistration.[18]

In the future, the authors intend to investigate the influence of these confounding effects through *in vitro* experimentation with excised cardiac tissue. Although such an experimental set-up will not mimic the important components inherent to the *in vivo* environment, it could allow for important investigation of structural (e.g., fiber orientation) and boundary condition (e.g., wall thickness) elements of the problem. The authors hope to improve the robustness of this acquisition technique by employing a greater number (i.e., >4) of parallel beam locations to be tracked simultaneously. This would serve to reduce acquisition time and could make tracking of a single wave response (as opposed to superposition of multiple responses) possible; a similar approach has been successively implemented in supersonic shear imaging.[6]

The authors also hope to acquire SWEI data at other portions of the cardiac cycle. Velocity estimates obtained during diastole *and* systole, for instance, could then be compared to the cyclic trends observed by Hsu et al and Sack et al.[11,14] And ultimately, in an effort to further understand how shear wave velocity through myocardium correlates to tissue mechanical properties and disease, the authors intend to apply these tracking techniques to a heart which is undergoing an induced chronic/acute failure state as part of a controlled animal study. In such a study, it may be possible to directly correlate shear wave velocity to a particular disease condition.

V. CONCLUSION

It is possible to generate and track ARFI-induced transverse mechanical waves in the mid-myocardium of a beating canine heart. Shear wave velocity estimates ranged from 0.82 to 2.65 m/s, which falls within the range of transverse wave speeds obtained by other research groups. It was also observed that velocity estimates could be made with good (i.e., coefficients of variation ≤ 19% for all matched acquisitions) beat-to-beat repeatability. A motion filter was successfully employed to reduce the physiological motion artifact; application of a motion filter appears necessary in some cases to obtain a reasonable velocity estimate. Trends in shear wave velocity estimates suggest a spatial dependence, with estimates changing through depth and lateral position. Continued investigation of potential confounding effects (e.g., anisotropy, wave type) must be pursued on *in vitro* and *in vivo* models. Additionally, a correlation between shear wave velocity and cardiac disease and/or tissue elasticity has yet to be firmly established. Despite these challenges, ARFI-driven shear wave velocimetry could offer a reliable, quantitative metric for clinically-relevant material properties of cardiac tissue in the future.

Acknowledgments

This work has been supported by NIH R21RB007741, NIH R01HL075485, and the NSF-GRFP, We thank the Ultrasound Business Unit of Siemens Healthcare for in-kind support, Ellen Dixon-Tulloch for surgical preparation, and Douglas Dumont for experimental assistance.

References

1. Westervelt PJ. The theory of steady forces caused by sound waves. J Acoust Soc Amer 1951;23:312–315.
2. Nightingale KR, Palmeri ML, Nightingale RW, Trahey GE. On the feasibility of remote palpation using acoustic radiation force. J Acoust Soc Amer 2001;110:625–34. [PubMed: 11508987]
3. Sarvazyan A, Rudenko O, Swanson S, Fowlkes J, Emelianov S. Shear wave elasticity imaging: A new ultrasonic technology of medical diagnostics. Ultrasound Med Biol 1998;24:1419–1435. [PubMed: 10385964]
4. Lai, W.; Rubin, D.; Krempl, E. Introduction to Continuum Mechanics. Butterworth-Heinmann,; Woburn, MA: 1999.
5. Bishop J, Poole G, Plewes D. Magnetic resonance imaging of shear wave propagation in excised tissue. J Magn Reson Imaging 1998;8:1257–1265. [PubMed: 9848738]
6. Bercoff J, Tanter M, Fink M. Supersonic shear imaging: a new technique for soft tissue elasticity mapping. IEEE Trans Ultrason Ferroelect Freq Contr 2004;51:396–409.
7. Tanter M, Bercoff J, Athanasiou A, et al. Quantitative assessment of breast lesion viscoelasticity: initial clinical results using supersonic shear imaging. Ultrasound Med Biol 2008;54:1373–1386. [PubMed: 18395961]
8. Palmeri ML, Wang MH, Dahl JJ, Frinkley KD, Nightingale KR. Quantifying hepatic shear modulus *In vivo* using acoustic radiation force. Ultrasound Med Biol 2008;34:546–558. [PubMed: 18222031]
9. D'Hooge J, Heimdal A, Jamal F, et al. Regional strain and strain rate measurements by cardiac ultrasound: principles, implementation and limitations. Eur J Echocardiogr 2000;1:154–170. [PubMed: 11916589]
10. Gilman G, Khandheria BK, Hagen ME, et al. Strain rate and strain: a step-by-step approach to image and data acquisition. J Am Soc Echocardiogr 2004;17:1011–1020. [PubMed: 15337972]
11. Hsu SJ, Bouchard RR, Dumont DM, Wolf PD, Trahey GE. *In vivo* assessment of myocardial stiffness with acoustic radiation force impulse imaging. Ultrasound Med Biol 2007;33:1706–1719. [PubMed: 17698282]
12. Kanai H. Propagation of spontaneously actuated pulsive vibration in human heart wall and *in vivo* viscoelasticity estimation. IEEE Trans Ultrason Ferroelect Freq Contr 2005;52:1931–1942.
13. Pernot M, Fujikura K, Fung-Kee-Fung SD, Konofagou EE. ECG-gated, mechanical and electromechanical wave imaging of cardiovascular tissues *in vivo*. Ultrasound Med Biol 2007;33:1075–1085. [PubMed: 17507146]
14. Sack I, Rump J, Elgeti T, Samani A, Braun J. MR elastography of the human heart: noninvasive assessment of myocardial elasticity changes by shear wave amplitude variations. Magn Reson Med 2008;61:668–677. [PubMed: 19097236]
15. Dahl JJ, Pinton GF, Palmeri ML, et al. A parallel tracking method for acoustic radiation force impulse imaging. IEEE Trans Ultrason Ferroelect Freq Contr 2007;54:301–312.
16. Bouchard RR, Hsu SJ, Dahl JJ, Palmeri ML, Trahey GE. Image quality, tissue heating, and frame-rate trade-offs in acoustic radiation force impulse imaging. IEEE Trans Ultrason Ferroelect Freq Contr 2009;56:63–76.
17. Gorcsan J, Gulati VK, Mandarino WA, Katz WE. Color-coded measures of myocardial velocity throughout the cardiac cycle by tissue Doppler imaging to quantify regional left ventricular function. Am Heart J 1996;131:1203–1213. [PubMed: 8644601]
18. Pinton GF, Dahl JJ, Trahey GE. Rapid tracking of small displacements with ultrasound. IEEE Trans Ultrason Ferroelect Freq Contr 2006;53:1103–1117.
19. Hsu SJ, Bouchard RR, Dumont DM, et al. Novel ARFI imaging methods for rapidly moving tissue. Ultrasonic Imaging 2009;31:195–210.

20. Viktorov, IA. Rayleigh and Lamb Waves: Physical Theory and Applications. Plenum Press; New York: 1967.

21. Streeter DD, Spotnitz HM, Patel DP, Ross J, Sonnenblick EH. Fiber orientation in the canine left ventricle during diastole and systole. Circ Res 1969;24:339–347. [PubMed: 5766515]

22. Gennisson JL, Catheline S, Chaffaï S, Fink M. Transient elastography in anisotropic medium: application to the measurement of slow and fast shear wave speeds in muscles. J Acoust Soc Amer 2003;114:536–541. [PubMed: 12880065]

23. Deffieux T, Montaldo G, Tanter M, Fink M. Shear wave spectroscopy for *in vivo* quantification of human soft tissues visco-elasticity. IEEE Trims Med Imaging 2009;28:313–322.

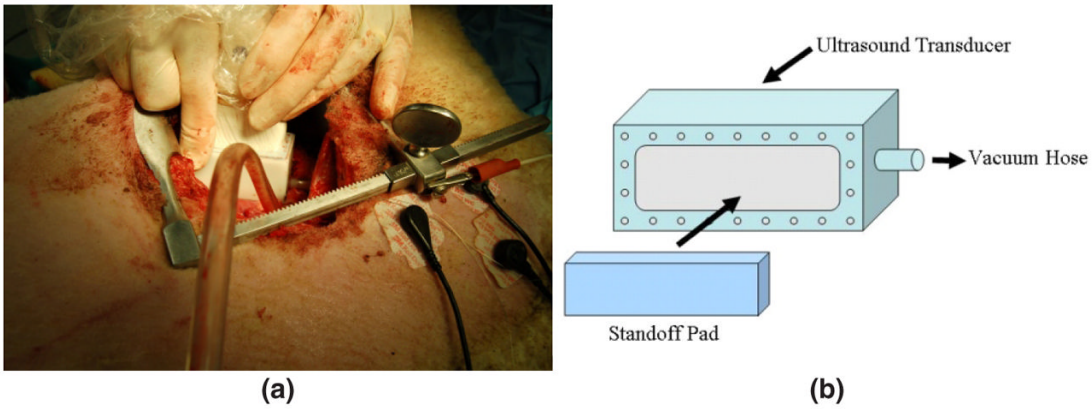

FIG. 1.

In vivo experimental set-up (a) and schematic of vacuum-coupling device (b). The image (a) depicts the experimental procedure following a thoracotomy, which provided direct access to the heart. The face of the transducer (located between the rib retractor) was secured to the surface of the epicardium with a vacuum-coupling device (white apparatus around transducer face; attached vacuum tube visible in foreground of image) that provided a 10-mm standoff. A schematic of the vacuum-coupling device (b) details the basic elements of this set-up component. The small holes bordering the standoff pad cutout generate a mild suction bond to the epicardial surface that helps to reduce lateral transducer motion during sequence acquisition.

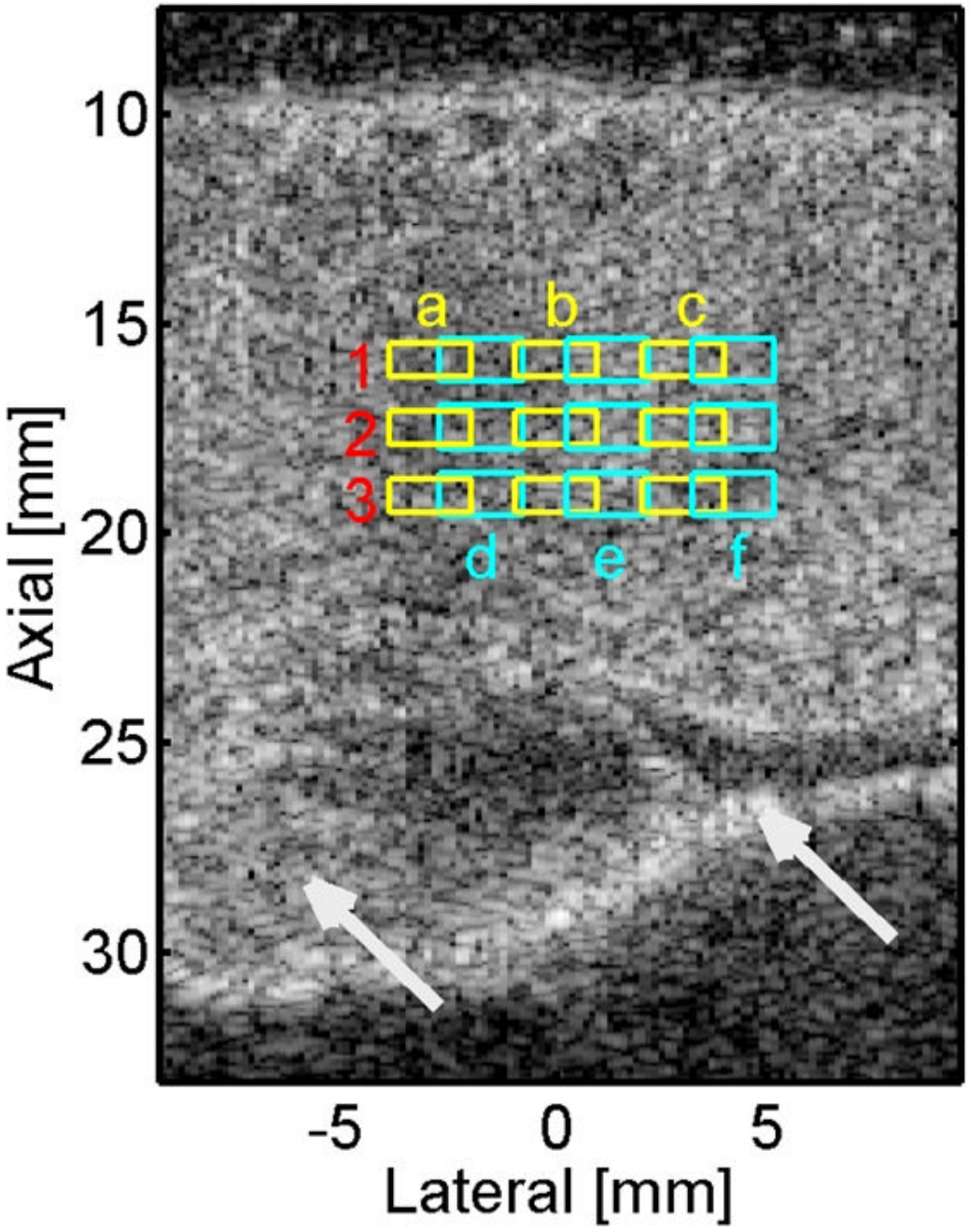

FIG. 2.

B-mode image of experimental field of view (FOV). The B-mode image depicts a portion of the LVFW (base-to-apex oriented right-to-left), with a papillary muscle (left-most arrow) and chordae tendineae (right-most arrow) visible in the lower portion of the image. Regions of displacement data included in shear wave velocimetry estimates are denoted with yellow or cyan boxes. Six ROIs are highlighted (a through c, denoted by yellow boxes; d through f, denoted by cyan boxes) with three independent depth kernels (denoted by red numbers) established for each. Kernels are 0.8 mm (height) by 1.9 mm (width); they are centered at 15.9, 17.5, and 19.1 mm depths and −3.0, −1.8, 0, 1.2, 3.0, and 4.2 mm lateral locations. The ARFI excitation for each of the six ROIs was focused at 17.5 mm and centered approximately 0.5

mm left of the leftmost lateral boundary of the defined ROI boxes. There are 14 evenly-spaced lateral tracking beams contained within each kernel.

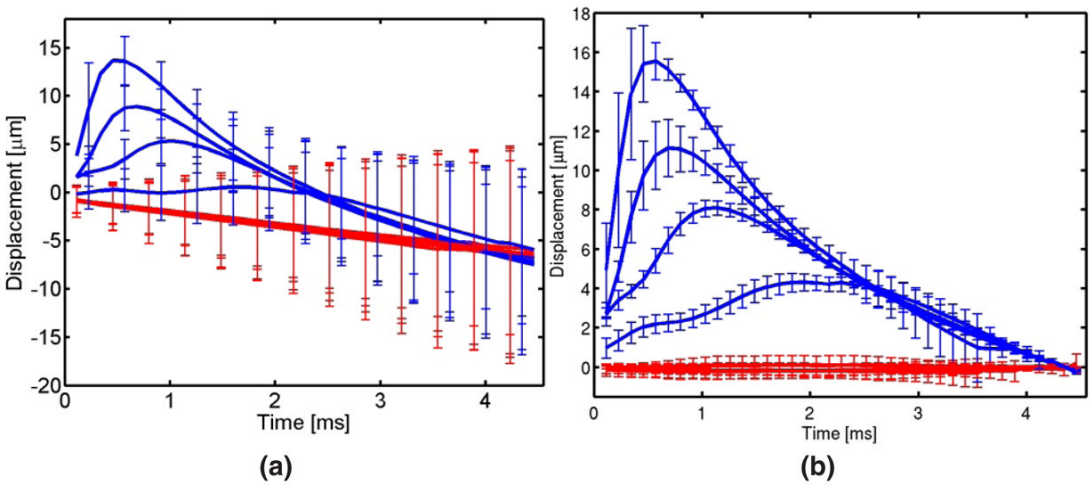

FIG. 3.

Displacement versus time data with (b) and without (a) motion filtering applied. In each plot, displacement data from SWEI sequences acquired with (blue) and without (red) active ARFI excitations (or 'pushes') are shown. Sequences were acquired in the LVFW of a canine subject during the mid-diastolic portion of the cardiac cycle. Data were obtained from the e-2 kernel depicted in figure 2. Means (N= 7) and SDs were calculated for the entire depth encompassed by e-2 and a represented for four lateral track locations (0.5, 0.8, 1.1, and 1.9mm) within this kernel through all tracked time, which starts following the initiation of the ARFI excitation transmit (which are zero-amplitude in the cases with no active push, i.e., the red traces), for both plots. In the active-push case with filtering (blue trace in 'b'), increasingly offset lateral locations correspond to traces with a peak mean displacement that occurs progressively later in time and with decreased amplitude. In the no-push case with filtering (red trace in 'b'), displacement traces from all four lateral locations are shown; no qualitative differences between them were observed. In both plots without filtering (a), similar trends exist despite being less apparent in the no-push case (blue trace). Note that data from fourteen lateral track locations (i.e., beams) was utilized for all linear regression fits; only four locations are depicted here for the sake of plot clarity. Additionally, only select error bars are displayed in 'a' for the sake of clarity.

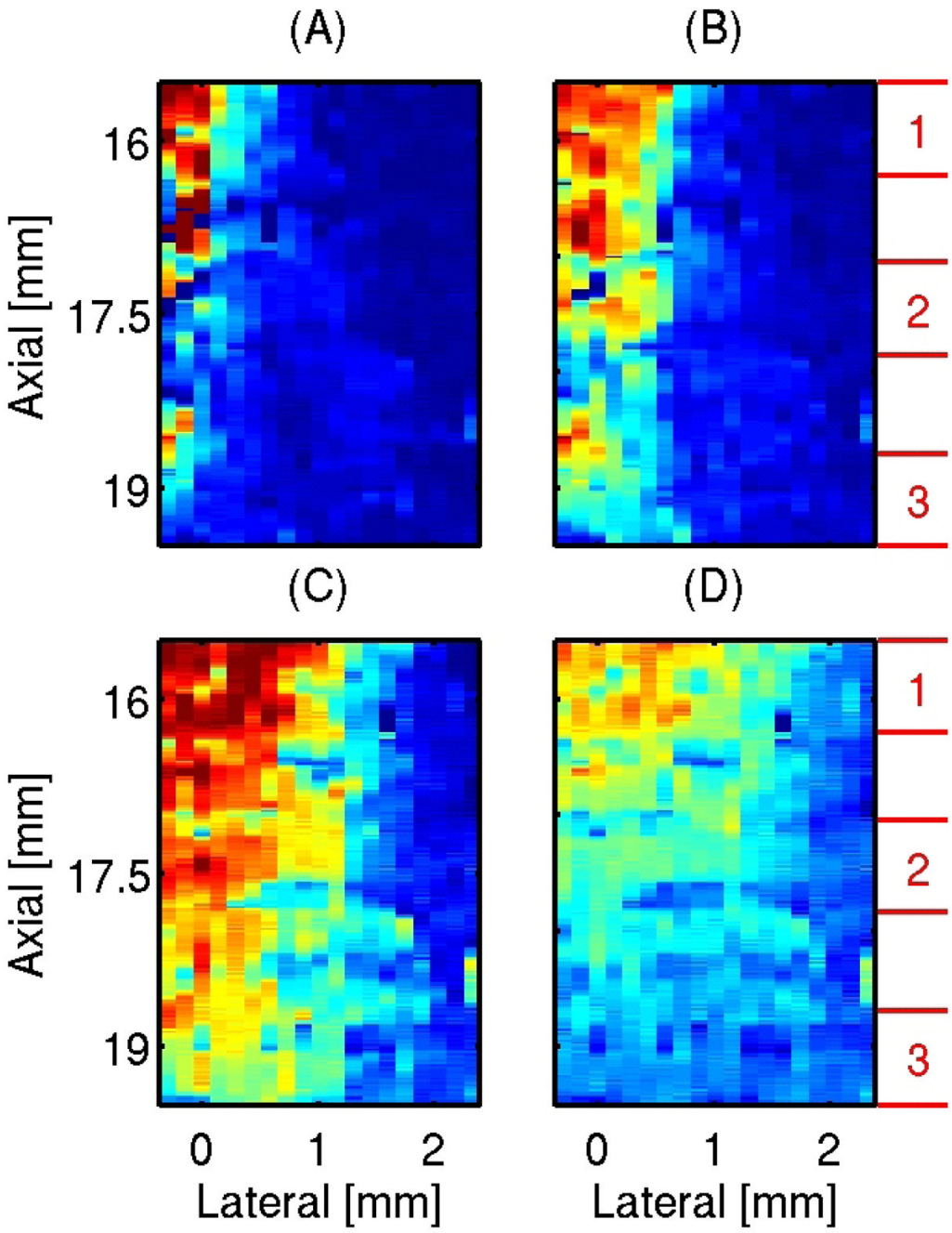

FIG. 4.

Displacement images at four specific times (1, 5, 13, and 21 ms for images A through D, respectively) following ARFI excitation. The displayed FOVs correlate to region ‘e’ in figure 2 but also include displacement estimates within the excitation volume (e.g., −0.3 to 0.2 mm, which is where displacement in image ‘A’ is predominately located). Depth kernels (as established by figure 2) are defined at the right of each image row in red. Note: two different dynamic ranges are employed: for images A and B, 0 (blue) to 30 (red) μm; for C and D, 0 to 15 μm.

TABLE 1

Displacement peak averages [μm] – Fig. 4.

Frame letter	A	B	C	D
Depth 1	26.5	24.4	15.0	10.3
Depth2	8.5	17.6	11.8	7.0
Depth 3	8.8	12.5	8.4	4.3

TABLE 2

Shear wave velocity [m/s] estimates – same location (‘e’).

Heartbeat [#]	1	2	3	4	5	6	7	μ±σ	R^2 value
Depth 1	0.97	0.91*	0.97	0.99	0.99	1.05	1.05	0.991–0.05	0.91±0.09
Depth 2	0.99	0.83	1.08	1.03	0.98	0.96	1.16	1.00±0.10	0.94±0.03
Depth 3	1.69	–	1.69	1.96	1.74	2.14	2.64	1.98±0.37	0.95±0.04

Ultrason Imaging. Author manuscript; available in PMC 2009 December 23.

TABLE 3

Shear wave velocity [m/s] estimates – different locations (‘a’–‘f’).

Heartbeat [#]	**1**	**2**	**3**	**4**	**5**	**6**	**7**
Region	**a**	**d**	**b**	**e**	**c**	**f**	**a**
Depth 1	**1.70**	*1.76*	**0.99**	*0.82*	**1.63**	*1.79*	**1.92**
Depth 2	**1.75**	*1.97*	**0.86**	*1.47*	**1.13**	*2.18*	**1.79**
Depth 3	**2.61***	*2.64*	–	–	–	*1.48*	**2.65**